

Weak phases production and heat generation controls fault friction during seismic slip

Hadrien Rattiez^{*,1} & Manolis Veveakis¹

¹*Civil and Environmental Engineering Department, Duke University*

The triggering and magnitude of earthquakes is determined by the friction evolution along faults. Experimental results have revealed a drastic decrease of the friction coefficient for velocities close to the maximum seismic one, independently of the material studied^{1,2}. Due to the extreme loading conditions during seismic slip, many competing physical phenomena are occurring (like mineral decomposition³, nanoparticle lubrication¹, melting⁴ among others) that are typically thermal in origin⁵ and are changing the nature of the material.

Here we show that a large set of experimental data for different rocks can be described by such thermally-activated mechanisms⁶, combined with the production of weak phases. By taking into account the energy balance of all processes during fault movement, we present a framework that reconciles the data, and is capable of explaining the frictional behavior of faults, across the full range of slip velocities ($10^{-9} - 10$ m/s).

The similarity of microstructures observed in nature and in experiments suggests that energetic frameworks like the one presented could quantitatively link observations across the scales and provide deep, physics-based insight on the physical mechanisms driving seismic slip.

20 **Introduction**

21 The knowledge of the friction (shear strength) evolution along a pre-existing fault is of major
22 importance, as it allows extracting many characteristics and features of seismic slip. In particular,
23 the decrease of the friction with increasing velocity or displacement (a process called frictional
24 weakening) determines the possible nucleation of earthquakes. If the weakening rate is larger than
25 a critical value determined by the release rate of elastic energy from the surrounding rock mass,
26 this leads to the triggering of a dynamic slip at the origin of earthquakes⁷. In addition to nucleation,
27 the evolution of the friction coefficient- and thus of the fault's shearing resistance- determines the
28 propagation and arrest of the fault slip and governs the form and budget of energy dissipation
29 during seismic slip⁸. The latter is essential as it determines the amount of energy dissipated at the
30 fault, which is radiated on the surface through seismic waves and tremors.

31 During the last 20 years, a large set of experimental works has been devoted to reproduc-
32 ing the extreme conditions of a seismic slip. The development of high velocity shear apparatus
33 allowed the research community to perform experiments at the maximum velocity reached during
34 an earthquake event (1 – 10 m/s) and, thus, characterize the behaviour of a fault over the full range
35 of possible slip rates⁹. A drastic decrease of the friction has been observed in most cases for
36 velocities closed to the maximum slip velocity independently of the material considered¹, however
37 the physical mechanisms accompanying this rapid weakening are different for each rock type. Fol-
38 lowing microstructural observations and measurements in the sheared samples, several thermally
39 and mechanically activated weakening mechanisms were proposed to understand the experimental

40 results at seismic slip rates⁶. The common feature of all these weakening mechanisms is a phase
41 transformation -like mineral decomposition³, nanoparticle lubrication¹, melting⁴- during which a
42 change in the nature of the material takes place.

43 **Modelling approach**

44 To describe the effect of such a weak phase on the frictional behaviour of a mixture of a strong/weak
45 phase and constrain the influence of phase change on the mechanical behaviour, we consider first
46 experiments looking at the effect of a weak phase on the frictional response of fault zones. The
47 weak phases used for the tests are talc or saturated clay materials sheared at low velocities (lower
48 than 10^{-5} m/s), so that the mechanisms described above are not triggered. The results are shown
49 in Figure 1, where we may observe that the friction coefficient μ decreases as the weak phase
50 fraction increases. This effect of the weak phase fraction can be captured using an exponential law
51 $\mu = \mu_0 + \Delta\mu e^{-\alpha w}$, where μ_0 is the friction coefficient of the weak phase, $\Delta\mu = \mu_s - \mu_0$ is the dif-
52 ference of the friction coefficient of the strong and weak phases, w is the weak phase fraction and
53 α a weakening coefficient ranging from 0.1 to 15 (see supplementary information). Note that such
54 nonlinear weakening laws are also used in geomechanical engineering to describe the weathering
55 of calcarenite^{10,11}.

56 The derived exponential decrease of the mechanical strength from the experimental data of
57 Figure 1 is then included into a thermo-chemo mechanical model that accounts for the coupled
58 mechanisms activated at higher velocity conditions (see Methods for the mathematical description

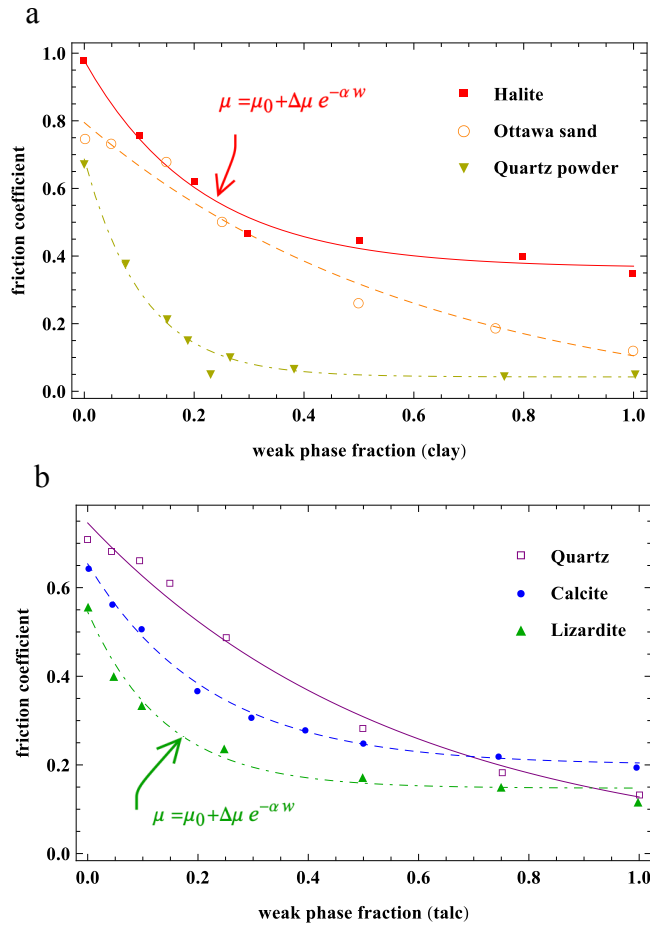


Figure 1: **Effect of the weak phase content on the steady state friction coefficient.** The friction of weak/strong phase binary mixtures is represented as function of the weak phase content in experiments carried out at subseismic sliding velocities and at constant normal stress using triaxial saw cut, double and simple direct shear and rotary shear configurations. **a**, results for clay as weak phase: red corresponds to a muscovite/halite mixture¹², orange to a crushed Ottawa sand/montmorillonite mixture¹³, dark yellow to a quartz powder/bentonite mixture¹⁴. **b**, results for talc as weak phase: purple corresponds to quartz as strong phase¹⁵, blue to calcite¹⁶, green to Lizardite¹⁵. In **a-b**, the points represent the experimental data and the solid or dashed lines represent the interpolation using this exponential function.

59 of the model). In this model, the degradation or creation of a weak phase is induced by the energy
60 input to the system and it is not present before shearing. This unifying approach aims at reconcil-
61 ing observations across a wide spectrum of materials and velocities. The extensive experimental
62 data set used for the comparison corresponds to shear tests performed with rotary shear apparatus
63 that allows to reach high displacements and therefore the steady state (see Figure 2). These exper-
64 iments are realized on either gouge granular samples (usually 1mm thick¹⁷) sandwiched between
65 two blocks or on bare rock samples¹⁸. In the latter, a gouge material is formed after only a few
66 millimetres of displacement² with a thickness of 100 to 300 μm . Data are gathered based on the
67 nature of the material sheared and the physical mechanisms that are inferred to operate during the
68 experiments^{1,19}.

69 The constitutive law for the mechanical behaviour is applied to the gouge material, which ac-
70 commodates all the deformation and is affected by the temperature, the weak phase fraction and the
71 state of stress. The weak phase creation is modelled as an endothermic first order chemical trans-
72 formation affecting the energy balance equation and respecting the mass balance. The geometry
73 of the model chosen is larger of one or two orders of magnitude than the gouge in order to impose
74 far field boundary conditions for the temperature and the extend of the phase transformation (see
75 Figure 2). The steady states of this model can be determined using a continuation algorithm (see
76 Methods), to test the hypothesis that the combination of thermally activated weakening and the
77 creation of a weak phase may account for the observed steady state frictional response over many
78 orders of magnitude of shear velocity.

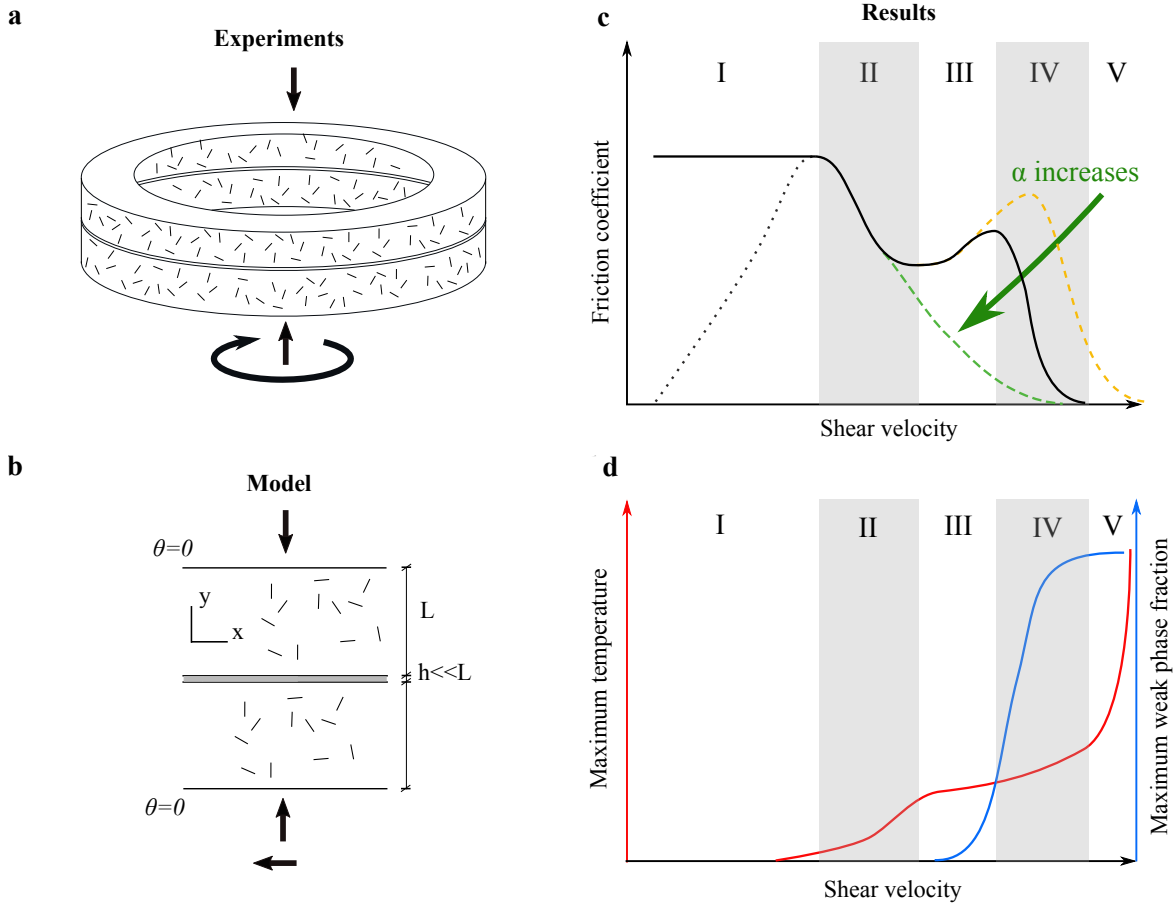


Figure 2: **a-b**, Schematic view of the geometry of the high velocity rotary shear experiments and the model. **c-d**, Steady state of the thermo-chemo mechanical model. Response of the mathematical system of equations (Eqs. 5-6 in Methods) at steady state. **c**, the steady state friction coefficient as a function of velocity, for varying weak phase sensitivity coefficient α . **d**, the steady-state temperature and weak phase content dependency on the velocity, plotted for the black line of **c**. The five regimes (I - V) that can be observed in the response of the friction coefficient are correlated with the temperature and weak phase production processes, as explained in the main text.

79 The resulting steady state response of the model, in terms of friction and velocity, is depicted
80 in Fig. 2. We can identify five distinct regimes of the system response to loading velocity: (I)
81 **Quasi-static.** At low velocities, the material strength is controlled by the quasi-static friction.
82 Negligible temperature increase or weak phase production is observed. (II) **Thermo-mechanical**
83 **weakening.** The temperature increase leads the friction coefficient to drop, in the absence of
84 any weak phase production. (III) **Thermo-chemical stabilization.** With increasing velocity and
85 temperature, small fractions of the weak phase are produced, absorbing the excess temperature
86 and reducing the thermal softening effect on the friction coefficient. Depending on the value of
87 the weakening coefficient, the friction coefficient can experience an intermediate increase. (IV)
88 **Chemo-mechanical weakening.** Eventually, weak phase content will be produced until it reaches
89 a critical value that will dominate the friction coefficient and lead the material to unconstrained
90 weakening. (V) **Runaway instability.** Once the reactants are depleted ($w = 1$), the temperature is
91 increasing uncontrollably and the friction coefficient drops towards zero.

92 **Results and discussion**

93 After identifying the regimes of the steady frictional response of faults, the model is applied to
94 experimental data. Figure 3 summarizes the results of the model for the steady state friction co-
95 efficient as a function of the velocity for six sets of materials^{1,9,18-21}. The experimental data are
96 a collection of several independent studies at different experimental conditions. As shown in the
97 supplementary information, the normal stress shows no clear effect on the evolution of the fric-
98 tion coefficient and, for this reason, it is not further investigated in this study. This is due to the

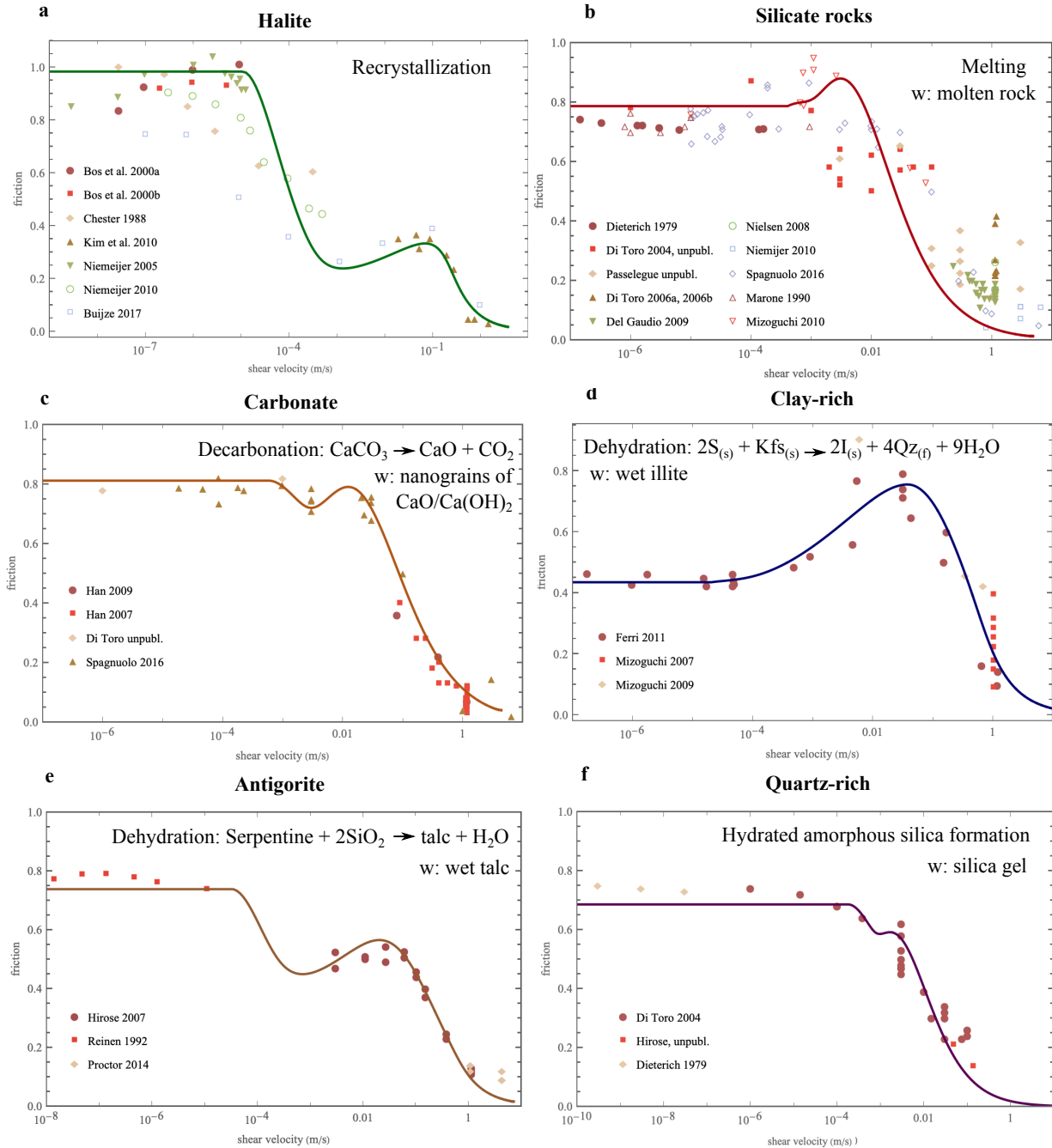


Figure 3: Results of the model for different types of materials. Application of the mathematical model (solid lines) to literature data (dots) of the friction coefficient as a function of the velocity. See the Methods for the mathematical description, Fig. 2 for the qualitative steady-state response and the supplementary information for the references of the experimental data. For each material, the phase transformation and the associated weak phase are indicated. **a**, for halite rocks. The model reproduces the experimental behaviour with $\alpha = 0$. **b**, for silicate rocks ($\alpha = 7.5$). **c**, for carbonate rocks ($\alpha = 5.3$). **d**, for clay-rich rocks ($\alpha = 2$). **e**, for antigorite ($\alpha = 1.5$). **f**, for quartz-rich rocks ($\alpha = 14$).

99 relatively low value of the normal stress that can be imposed for high velocity experiments (≤ 20
100 MPa). However, the normal stress is expected to play an important role on the fault's behavior
101 by affecting the temperature increase or phase transitions. This effect could be taken into account
102 with this model by considering a dependency of the thermal and chemical activation enthalpies on
103 the normal stress²²⁻²⁴.

104 One of the interesting features of the model is the reproduction of strengthening observed
105 experimentally at intermediate velocities (regime III in Figure 2) without supposing any additional
106 hardening mechanism. This rehardening is achieved when the energetics of the phase transition
107 and mechanical response are different enough so that temperature can be increased without weak
108 phase production. When this is not the case, the intermediate regimes of the model are not distinct,
109 as shown in Figure 2c, 3c and 3f.

110 For each material, the inferred phase transformation and the resulting weak product are high-
111 lighted based on experimental observations. However, for most of them (except when melt is cre-
112 ated), there is no general agreement about which phase transition is at the origin of the weakening.
113 Indeed, several mechanisms are usually triggered and it is difficult to isolate the effect of each
114 one of them. In addition, there might be microstructural features and unstable phases produced
115 during high velocity slip that leaves little or none evidence in the microstructure after the exper-
116 iment. Nevertheless, the model enables to capture accurately the microstructural observations,
117 when available, and uses as input the material parameters listed in the supplementary information.
118 Also, it enables us to retrieve information for the parameters of the different processes such as the

119 activation energies, together with an assessment of the temperature evolution. This can be used
120 as a basis to compare with the microstructural observations of the samples after the experiments.
121 Indeed, in Figure 4 we are summarizing the evolution of the Temperature and weak phase ratio w
122 required to obtain the friction coefficient results of Figure 3. Based on these two figures, we can
123 compile the processes underpinning the macroscopic response of the frictional resistance of the
124 different materials.

125 The temperature predicted by the model when the weak phase begins to appear can be
126 compared to the theoretical activation temperature of the phase transformation (decarbonation²⁵,
127 melting²⁶, dehydration²⁷ or clay type transition⁹), when available. In all cases, the temperature of
128 the model is lower than the theoretical one (e.g. 530° C against 720° C for carbonates) implying
129 that the phase transition is initiated locally at the contact of the grains where the temperature can
130 be higher than the bulk temperature (a process called flash heating⁵ that depends on the asperity
131 size distribution). For silicate rocks, an unique set of parameters has been used. It is a strong
132 assumption as the melting temperature depends on the silica content, which is different for Gab-
133 bro, Peridotite or Granite, and this effect should be taken into account for a finer description of
134 this set of experiments. The melting temperature reported in Figure 4d, is the melting tempera-
135 ture of Gabbro²⁶. The local phase changes are often hard to detect even though essential for the
136 mechanical behaviour. This also explains why the evidences of the phase transformations from
137 specific sensors or microstructural observations (recrystallized halite grains¹⁷, increase of CO₂²⁵
138 or humidity next to the tested sample¹⁸, melted asperities²⁸ and white flakes due to silica gel²⁰) are
139 retrieved for higher velocities in experiments than predicted by the model.

140 A notable case is halite, for which the weakening factor that enables a better fit of the data is
141 $\alpha = 0$ implying that any weak phase generated during shear does not affect the friction coefficient.
142 This is inferred here to happen because the material undergoes recrystallisation¹⁷ during shearing,
143 which is a phase transformation that produces the same mineral with different grain sizes. Despite
144 not producing a weak phase directly though, recrystallisation affects the energy budget and, thus
145 the temperature produced (Figure 4) and therefore the mechanical behaviour of the gouge. How-
146 ever, for this material, localized melting of halite may also have occurred²⁹, and microstructural
147 evidences may have been erased by recrystallization¹⁷.

148 For serpentine rocks and clay-rich (smectite) gouges, the increase of temperature with ve-
149 locity induces a dehydration of the material that can be evidenced by the presence of talc or illite.
150 Yet, dry illite has a higher shear strength than dry smectite³⁰ and pure dry talc is a weak phase at
151 low velocities but not for high velocities³¹. However, the phase transformation in these two cases
152 involves also the release of water. The mixture of talc with water presents a friction coefficient of
153 0.2, almost independently of the velocity³¹. Also, the large amount of water produced by smectite-
154 dehydration induces the illite to present a water content larger than the Atterberg's liquid limit and,
155 thus, behaves like a fluid. Therefore, in the cases of serpentinite and Smectite, the weak phase is
156 likely to be the mixture of the dehydration product and water.

157 There are many evidences of decarbonization during shearing of carbonate rocks at high
158 velocities³². A significant increase of CO₂ has been detected by electrolyte-type sensors near
159 high-velocity experiments and microstructural observations have shown the presence of very fine-

160 grained powders of lime (CaO) and portlandite (hydrated lime). For this material, the weakening
161 has been attributed to the effect of the thermal decomposition of carbonates into nanograins of lime
162 and CO₂^{25,32}, but the microphysics of the weakening is not yet fully understood⁶.

163 These results suggest that heating produced during shear and phase transformations of the
164 material inside the gouge may be the dominant mechanisms during slip in dry conditions. The
165 physics-based model presented here enables us to isolate the main physical mechanisms and con-
166 strain the parameter's values. The knowledge of the variations of these parameters with the normal
167 stress and sample size would allow to extrapolate experimental results to conditions *in-situ*. How-
168 ever, in natural conditions faults are rarely dry and are usually saturated with pressurized fluids, a
169 scenario difficult to study experimentally at high velocity². The presence of fluids can trigger other
170 mechanisms like cavitation³³, pressure-solution³⁴⁻³⁶ or thermal pressurization³⁷⁻⁴⁰. The addition of
171 such mechanisms could in turn either change the steady state response of the system or induce tran-
172 sients which could drive the system far from its steady-state response^{27,41}. In that case a detailed
173 model based on the results of high velocity dry experiments and saturated low velocity experiments
174 needs to be carried to assess the dominant mechanisms of slip and earthquake nucleation.

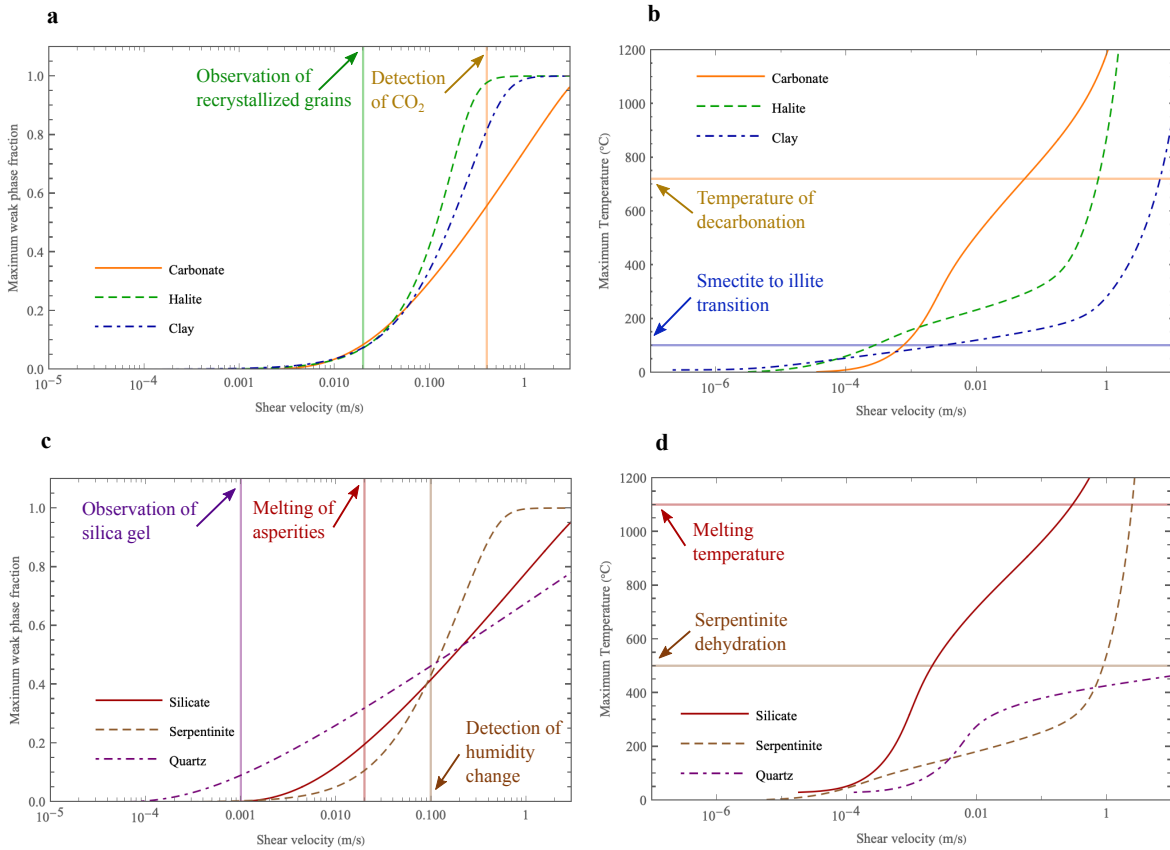


Figure 4: **Temperature and weak phase fraction evolution with the velocity for the experiments of Fig. 3.** **a** and **c**, weak phase fraction in the middle of the sample. Note that weak phase production has been approached as a first order chemical reaction, thus reaching its maximum value of one (100% weak phase present) when the reaction is depleted. **b** and **d**, maximum temperature in the middle of the sample.

175 **Methods**

176 **Description of the Mathematical Model.** When the shear velocity applied to a rock or a granular
177 sample is increased, thermal effects tend to dominate the frictional response^{5,20,42,43}. A critical
178 velocity is required to activate this mechanism that is related to the processes at asperities or grain
179 contacts⁵. In this paper, we focus on the response of the material for intermediate and high veloc-
180 ities where the thermal and chemical effect are important (other models have been developed for
181 lower velocities and the nucleation of earthquakes^{42,44}). Therefore, we consider here that for low
182 velocities experiments the strength of the material is determined by the static friction of the ma-
183 terials in contact or the internal static friction of the granular assembly. For velocities larger than
184 the critical one, the shear stress of the system is calculated by solving a thermo-chemo-mechanical
185 model inside the deforming zone. The critical velocity is retrieved as a result from this model
186 and can be approximated by an analytical solution (see supplementary information). Physically, it
187 corresponds to the critical velocity for which thermal weakening becomes significant.

188 The mathematical model consists of solving the momentum, mass and energy balance equa-
189 tion at steady state, for an infinite sheared layer. The equations are briefly summarized here for
190 easiness in reproducibility of the results³.

191 The momentum balance equations are considered and we neglect the inertia terms⁴⁵:

$$\sigma_{ij,j} = 0 \quad (1)$$

192 where σ_{ij} is the stress tensor. These equations lead in the case of one dimensional shear zone to a
193 constant normal and shear stress in space inside the layer.

194 The constitutive law for the mechanical behaviour is a rigid elastic-viscoplastic law with
 195 the most generic form: an Arrhenius-power law dependency^{3,46}. This law is only considered in
 196 a layer of thickness h , much smaller than the total thickness of the layer L (see Figure 2). This
 197 enables to describe the fact that after only a few millimetres of slip during the shear experiments
 198 on bare rocks, a thin layer of gouge materials forms. This layer composed of crushed grains from
 199 the initially rough surfaces has generally a thickness of 100-300 μm^2 and accommodates all the
 200 deformation. However, as the boundary conditions for the weak phase and the temperature are
 201 not well defined for this gouge layer, a domain of 1 cm is considered in order to apply Dirichlet
 202 boundary conditions for these fields.

$$\dot{\epsilon}^{vp} = \dot{\epsilon}^0 \left(\frac{\tau}{\tau_y} \right)^m e^{-Q/RT} \quad (2)$$

203 where $\dot{\epsilon}^0$ is a reference strain rate, m is the exponent of the power law, τ is the shear stress, τ_y is
 204 the yield stress, Q is an activation enthalpy for the microscopic mechanism inducing a nonlinear
 205 behaviour, R is the perfect gas constant and T is the temperature. This law allows to include more
 206 physics into the hardening evolution as in the theory of plasticity for metals⁴⁶. The Arrhenius
 207 dependency of the flow law enables to introduce multi-physical couplings such as the effect of
 208 heat generation on the frictional strength or more generally interface phenomena between the solid
 209 skeleton and the pores^{47,48}. In principle, $\dot{\epsilon}^0$ and Q are functions of internal state variables ξ , that
 210 are representative of mechanisms like grain size sensitivity (in which case an expression of the
 211 average grain size is the internal state variable), fugacity sensitivity, effect of asperities of the
 212 contacts etc. Such dependencies would require additional evolution laws for the internal state
 213 variables $\dot{\xi} = f(\xi, T, \dots)$, accompanying Eq. (2). However, since in this work we focus on the

214 steady state response of the material (i.e. $\dot{\xi} = 0$), these evolution laws provide constant (arbitrary)
 215 values of the internal state variables, that can in turn be lumped into $\dot{\epsilon}^0$ and Q .

216 The effect of the non-mechanical state variables on the mechanical behaviour of the system
 217 can be expressed as a single scalar function called the weathering index¹¹, X_d . The strength of the
 218 material depends on both the plastic strain and this weathering index. It is assumed that the two
 219 effects are uncoupled^{10,11} and a multiplicative structure of the yield stress is postulated:

$$\tau_y = T_y(\epsilon^p)T_y(X_d) \quad (3)$$

220 In our case, we do not consider any purely mechanical hardening law, so that the function $T_y(\epsilon^p)$ is
 221 constant. Moreover, X_d is considered to be a weak phase volume fraction. As shown in Figure 1,
 222 the presence of a weak phase induces an exponential decrease of the frictional strength along with
 223 the weak phase fraction. Assuming negligible shear strength for the weak phase, the final form of
 224 the constitutive law is therefore:

$$\dot{\epsilon}^{vp} = \dot{\epsilon}^0 \left(\frac{\tau}{\tau_0} \right)^m e^{-Q/RT} e^{\alpha m w} \quad (4)$$

225 where τ_0 is the yield strength of the strong phase and α is the weak phase sensitivity coefficient.

226 From this equation, the friction is determined by:

$$\mu = \frac{\tau}{\sigma} = \frac{\tau_0}{\sigma} \left(\frac{\dot{\epsilon}^{vp}}{\dot{\epsilon}^0} \right)^{1/m} e^{Q/mRT} e^{-\alpha w} \quad (5)$$

227 where σ is the normal stress applied to the layer.

228 For a material consisting of two species: a weak and a strong phase, occupying volumes V_w
 229 and V_s respectively, we may define the volume ratio $w = \frac{V_w}{V_w + V_s}$. Inside a one dimensional shear

230 zone yield a system of two equations^{3,49} obtained from the mass balance of the weak phase fraction
 231 and the energy balance equations:

$$\frac{\partial T}{\partial t} = c_{th} \frac{\partial^2 T}{\partial y^2} + F(y) \frac{\tau \dot{\epsilon}^{vp}}{\rho C} - \frac{\Delta H}{\rho C} r_F \quad (6)$$

$$\frac{\partial \rho_1}{\partial t} + \frac{\partial J_w}{\partial y} = r_F \quad (7)$$

232 where T is the temperature, c_{th} the thermal diffusivity, ρC the heat capacity of the mixture con-
 233 sidered constant here, J_w the diffusion flux of the weak phase, ΔH the enthalpy of the phase
 234 change reaction considered endothermic, r_F the reaction rate and $\rho_1 = \rho_w w$. $F(y)$ is a function
 235 which value is 1 for $y \in [-h/2, h/2]$ and 0 otherwise. The reaction rate is expressed as first order
 236 chemical reaction with an Arrhenius law.

$$r_F = (1 - w) \frac{\rho_s}{M_s} k_F e^{-Q_c/RT} \quad (8)$$

237 where ρ_s and M_s are the density and molar mass of the strong phase. k_F and Q_c are the preexpo-
 238 nential factor and activation energy of the chemical reaction. Using Equations 4, 8, considering a
 239 Fick's law for the diffusion flux (defining a diffusivity c_w) and the steady state of Equations 6 and
 240 7, we obtain a system of two differential equations in space. This system is written in a dimension-
 241 less form for the purpose of reducing the number of parameters to study and to enable a clearer
 242 understanding of the main features of the system:

$$\frac{\partial^2 \theta}{\partial \bar{y}^2} + F(\bar{y}) Gr e^{\frac{Ar \theta}{1+\theta}} e^{\alpha m w} - Da(1 - w) e^{\frac{Arc \theta}{1+\theta}} = 0 \quad (9)$$

$$\frac{\partial w}{\partial \bar{y}^2} + \beta Da(1 - w) e^{\frac{Arc \theta}{1+\theta}} = 0 \quad (10)$$

243 where, θ is the dimensionless temperature. Gr , Da , Ar and Arc are called the Gruntfest, Damköhler,

244 Arrhenius and chemical Arrhenius numbers respectively. They are defined by:

$$Ar = \frac{Q}{R T_0}, \quad Arc = \frac{Qc}{R T_0} \quad (11)$$

$$Gr = \frac{\tau_0 \dot{\epsilon}^0 L^2}{\rho C c_{th} T_0} \left(\frac{\tau}{\tau_0}\right)^{m+1} e^{-Ar} \quad (12)$$

$$Da = \frac{\Delta H k_F \rho_s L^2}{\rho C M_s c_{th} T_0} e^{-Arc} \quad (13)$$

$$\beta = \frac{\rho C c_{th} T_0 M_w}{\Delta H \rho_w c_w} \quad (14)$$

245 **Numerical Bifurcation of the Steady State friction coefficient.** The solutions of this nonlinear
 246 system of differential equations are approximated numerically using pseudospectral methods. The
 247 temperature and weak phase fraction fields are interpolated in space using Chebyshev polynomials
 248 of the first kind:

$$\theta(\bar{y}) = \sum_{i=1}^N a_i (\phi_{2i}(\bar{y}) - 1) \quad (15)$$

$$w(\bar{y}) = \sum_{i=1}^N b_i (\phi_{2i}(\bar{y}) - 1) \quad (16)$$

249 where ϕ_{2i} are the Chebyshev polynomials of degree $2i$. Note that only the even degree Chebyshev
 250 polynomials are kept here as the solution is symmetric about the origin. Moreover, a basis recom-
 251 bination is used by considering interpolation functions of the form $\psi_{2i}(y) = \phi_{2i}(y) - 1$, allowing
 252 to enforce a zero Dirichlet boundary conditions implicitly⁵¹. N is the number of polynomials used
 253 to simulate the solutions. A convergence analysis has been conducted in each case to verify that N
 254 is high enough to have a negligible error on the solution. a_i and b_i are the interpolation coefficients
 255 for the temperature and the weak phase fraction respectively. The interpolation points used for the
 256 resolution are the Gauss-Lobato points defined by:

$$x_j = \cos\left(\frac{(2j-1)\pi}{4N}\right), \quad j = 1, \dots, N \quad (17)$$

257 The nonlinear system of algebraic equations obtained is solved using the Newton-Raphson method.
258 In order to capture all the steady state solutions of the system for the different values of the stress, a
259 continuation pseudo-arclength algorithm is used. The continuation parameter chosen is the Grunt-
260 fest number³.

- 262 1. Di Toro, G. *et al.* Fault lubrication during earthquakes. *Nature* **471**, 494–498 (2011). URL
263 <http://www.nature.com/doifinder/10.1038/nature09838>.
- 264 2. Reches, Z. & Lockner, D. A. Fault weakening and earthquake in-
265 stability by powder lubrication. *Nature* **467**, 452–455 (2010). URL
266 <http://www.nature.com/doifinder/10.1038/nature09348>.
- 267 3. Veveakis, E. *et al.* Chemical reaction capping of thermal instabilities during shear of
268 frictional faults. *Journal of the Mechanics and Physics of Solids* **58**, 1175–1194 (2010). URL
269 <http://www.sciencedirect.com/science/article/pii/S0022509610001262>.
- 270 4. Di Toro, G., Pennacchioni, G. & Teza, G. Can pseudotachylytes be used to infer earthquake
271 source parameters? An example of limitations in the study of exhumed faults. *Tectonophysics*
272 **402**, 3–20 (2005).
- 273 5. Rice, J. R. Heating and weakening of faults during earthquake slip. *Journal of Geophysical*
274 *Research: Solid Earth* **111** (2006).
- 275 6. Niemeijer, A. *et al.* Inferring earthquake physics and chemistry using an integrated field and
276 laboratory approach. *Journal of Structural Geology* **39**, 2–36 (2012).

277
278
279
280
281
282
283
284
285
286
287
288
289
290
291
292
293
294
295

7. Scholz, C. H. *The mechanics of earthquakes and faulting* (Cambridge, 2002), second edi edn.
8. Kanamori, H. & Brodsky, E. E. The physics of earthquakes. *Reports on Progress in Physics* **67**, 1429–1496 (2004).
9. Ferri, F. *et al.* Low- to high-velocity frictional properties of the clay-rich gouges from the slipping zone of the 1963 Vaiont slide, northern Italy. *Journal of Geophysical Research: Solid Earth* **116**, 1–17 (2011).
10. Ciantia, M. O. & Hueckel, T. Weathering of submerged stressed calcarenites: chemo-mechanical coupling mechanisms. *Géotechnique* **63**, 768–785 (2013).
11. Nova, R., Castellanza, R. & Tamagnini, C. A constitutive model for bonded geomaterials subject to mechanical and/or chemical degradation. *International Journal for Numerical and Analytical Methods in Geomechanics* **27**, 705–732 (2003). URL <http://doi.wiley.com/10.1002/nag.294>.
12. Niemeijer, A. R. & Spiers, C. J. Influence of phyllosilicates on fault strength in the brittle-ductile transition: insights from rock analogue experiments. *Geological Society, London, Special Publications* **245**, 303–327 (2005). URL <http://books.google.com/books?hl=en&lr=&id=1oMGwL8ExU0C&oi=fnd&pg=PA303&>
13. Tembe, S., Lockner, D. A. & Wong, T. F. Effect of clay content and mineralogy on frictional sliding behavior of simulated gouges: Binary and ternary mixtures of quartz, illite, and montmorillonite. *Journal of Geophysical Research: Solid Earth* **115**, 1–22 (2010).

- 296 14. Oohashi, K., Hirose, T., Takahashi, M. & Tanikawa, W. Dynamic weakening of smectite-
297 bearing faults at intermediate velocities: Implications for subduction zone earthquakes. *Jour-*
298 *nal of Geophysical Research : Solid Earth* **120**, 1572–1586 (2015).
- 299 15. Moore, D. E. & Lockner, D. A. Frictional strengths of talc-serpentine and talc-quartz mixtures.
300 *Journal of Geophysical Research: Solid Earth* **116**, 1–17 (2011).
- 301 16. Giorgetti, C., Carpenter, B. M. & Collettini, C. Frictional behavior of talc-calcite mixtures.
302 *Journal of Geophysical Research: Solid Earth* **120**, 6614–6633 (2015).
- 303 17. Buijze, L., Niemeijer, A. R., Han, R., Shimamoto, T. & Spiers, C. J. Friction
304 properties and deformation mechanisms of halite(-mica) gouges from low to high slid-
305 ing velocities. *Earth and Planetary Science Letters* **458**, 107–119 (2017). URL
306 <http://dx.doi.org/10.1016/j.epsl.2016.09.059>.
- 307 18. Hirose, T. & Bystricky, M. Extreme dynamic weakening of faults during dehydration by
308 coseismic shear heating. *Geophysical Research Letters* **34**, 10–14 (2007).
- 309 19. Spagnuolo, E., Nielsen, S., Violay, M. & Di Toro, G. An empirically based steady state friction
310 law and implications for fault stability. *Geophysical Research Letters* **43**, 3263–3271 (2016).
- 311 20. Di Toro, G., Goldsby, D. L. & Tullis, T. E. Friction falls towards zero in quartz rock as slip
312 velocity approaches seismic rates. *Nature* **427**, 436–439 (2004).
- 313 21. Hirose, T., Mizoguchi, K. & Shimamoto, T. Wear processes in rocks at slow
314 to high slip rates. *Journal of Structural Geology* **38**, 102–116 (2012). URL
315 <http://dx.doi.org/10.1016/j.jsg.2011.12.007>.

- 316 22. Shun-ichiro Karato. *Deformation of Earth Materials: An Introduction to the Rheology of Solid*
317 *Earth* (2008). URL www.cambridge.org.
- 318 23. Kelka, U., Veveakis, M., Koehn, D. & Beaudoin, N. Zebra rocks: Com-
319 paction waves create ore deposits. *Scientific Reports* **7**, 1–9 (2017). URL
320 <http://dx.doi.org/10.1038/s41598-017-14541-3>.
- 321 24. Alevizos, S. *et al.* A Framework for Fracture Network Formation in Overpressurised Imper-
322 meable Shale: Deformability Versus Diagenesis. *Rock Mechanics and Rock Engineering* **50**,
323 689–703 (2017).
- 324 25. Han, R., Shimamoto, T., Hirose, T., Ree, J. H. & Ando, J. Ultralow friction of carbonate faults
325 caused by thermal decomposition. *Science* **316**, 878–881 (2007).
- 326 26. Hirose, T. & Shimamoto, T. Growth of molten zone as a mechanism of slip weakening of
327 simulated faults in gabbro during frictional melting. *Journal of Geophysical Research: Solid*
328 *Earth* **110**, 1–18 (2005).
- 329 27. Poulet, T., Veveakis, M., Regenauer-Lieb, K. & Yuen, D. A. Thermo-poro-mechanics of
330 chemically active creeping faults : 3 . The role of serpentinite in episodic tremor and slip
331 sequences , and transition to chaos. *Journal of Geophysical Research* **119**, 4606–4625 (2014).
- 332 28. Goldsby, D. L. & Tullis, T. E. Flash Heating Leads to Low Frictional Earthquake Slip Rates.
333 *Science* **334**, 216–218 (2011).

- 334 29. Kim, J. W., Ree, J. H., Han, R. & Shimamoto, T. Experimental evidence for the simultaneous
335 formation of pseudotachylyte and mylonite in the brittle regime. *Geology* **38**, 1143–1146
336 (2010).
- 337 30. Saffer, D. M. & Marone, C. Comparison of smectite- and illite-rich gouge frictional properties:
338 Application to the updip limit of the seismogenic zone along subduction megathrusts. *Earth
339 and Planetary Science Letters* **215**, 219–235 (2003).
- 340 31. Chen, X., Elwood Madden, A. S. & Reches, Z. The frictional strength of talc gouge in high-
341 velocity shear experiments. *Journal of Geophysical Research: Solid Earth* 1–16 (2017). URL
342 <http://doi.wiley.com/10.1002/2016JB013676>.
- 343 32. Han, R., Hirose, T. & Shimamoto, T. Strong velocity weakening and powder lubrication of
344 simulated carbonate faults at seismic slip rates. *Journal of Geophysical Research: Solid Earth*
345 **115** (2010).
- 346 33. Verberne, B. A. *et al.* Microscale cavitation as a mechanism for nucleating earth-
347 quakes at the base of the seismogenic zone. *Nature Communications* **8** (2017). URL
348 <http://dx.doi.org/10.1038/s41467-017-01843-3>.
- 349 34. Bos, B., Peach, C. J. & Spiers, C. J. Slip behavior of simulated gouge-bearing faults under
350 conditions favoring pressure solution. *Journal of Geophysical Research: Solid Earth* **105**,
351 16699–16717 (2000).

- 352 35. Guevel, A., Rattetz, H. & Veveakis, M. Contact phase-field modeling for chemo-mechanical
353 degradation processes. Part II: Numerical applications with focus on pressure solution.
354 *Preprint arXiv* (2019).
- 355 36. Rattetz, H., Disidoro, F., Sulem, J. & Veveakis, M. Influence of dissolution on the frictional
356 properties of carbonate faults. *Geomechanics for Energy and the Environment* (2019).
- 357 37. Viesca, R. C. & Garagash, D. I. Ubiquitous weakening of faults due
358 to thermal pressurization. *Nature Geoscience* **8**, 875–879 (2015). URL
359 <http://www.nature.com/doi/10.1038/ngeo2554>.
- 360 38. Rattetz, H., Stefanou, I. & Sulem, J. The importance of Thermo-Hydro-Mechanical couplings
361 and microstructure to strain localization in 3D continua with application to seismic faults. Part
362 I: Theory and linear stability analysis. *Journal of the Mechanics and Physics of Solids* **115**,
363 54–76 (2018).
- 364 39. Rattetz, H., Stefanou, I., Sulem, J., Veveakis, M. & Poulet, T. The importance of Thermo-
365 Hydro-Mechanical couplings and microstructure to strain localization in 3D continua with
366 application to seismic faults . Part II : Numerical implementation and post-bifurcation analysis.
367 *Journal of the Mechanics and Physics of Solids* **115**, 1–29 (2018).
- 368 40. Rattetz, H., Stefanou, I., Sulem, J., Veveakis, M. & Poulet, T. Numerical Analysis of Strain
369 Localization in Rocks with Thermo-hydro-mechanical Couplings Using Cosserat Continuum.
370 *Rock Mechanics and Rock Engineering* **51**, 3295–3311 (2018).

- 371 41. Veveakis, M., Poulet, T. & Alevizos, S. Thermo-poro-mechanics of chemically active creeping
372 faults: 2. Transient considerations. *Journal of Geophysical Research: Solid Earth* n/a–n/a
373 (2014).
- 374 42. Chen, J., Niemeijer, A. R. & Spiers, C. J. Microphysically Derived Expressions for Rate-and-
375 State Friction Parameters, a , b , and D_c . *Journal of Geophysical Research: Solid Earth* **122**,
376 9627–9657 (2017).
- 377 43. Proctor, B. P. *et al.* Dynamic weakening of serpentinite gouges and bare surfaces at seismic
378 slip rates. *Journal of Geophysical Research : Solid Earth* **119**, 8107–8131 (2014).
- 379 44. Aharonov, E. & Scholz, C. H. A Physics-Based Rock Friction Constitutive Law: Steady State
380 Friction. *Journal of Geophysical Research: Solid Earth* **123**, 1591–1614 (2018).
- 381 45. Rice, J. R., Rudnicki, J. W. & Platt, J. D. Stability and localization of rapid shear in fluid-
382 saturated fault gouge : 1 . Linearized stability analysis. *Journal of Geophysical Research*
383 1–23 (2014).
- 384 46. Frost, H. J. & Ashby, M. F. *Deformation-Mechanism Maps, The Plasticity and Creep of Metals*
385 *and Ceramics* (Pergamon Press, 1982).
- 386 47. Einav, I. The unification of hypo-plastic and elasto-plastic theories. *In-*
387 *ternational Journal of Solids and Structures* **49**, 1305–1315 (2012). URL
388 <http://dx.doi.org/10.1016/j.ijsolstr.2012.02.003>.

- 389 48. Veveakis, E. & Regenauer-Lieb, K. Cnoidal waves in solids. *Jour-*
390 *nal of the Mechanics and Physics of Solids* **78**, 231–248 (2015). URL
391 <http://dx.doi.org/10.1016/j.jmps.2015.02.010>.
- 392 49. Sulem, J. & Famin, V. Thermal decomposition of carbonates in fault zones: Slip-weakening
393 and temperature-limiting effects. *Journal of Geophysical Research* **114**, 1–14 (2009).
- 394 50. Green II, H. W., Shi, F., Bozhilov, K., Xia, G. & Reches, Z. Phase transformation and nano-
395 metric flow cause extreme weakening during fault slip. *Nature Geoscience* **8**, 484–489 (2015).
- 396 51. Boyd, J. P. *Chebyshev and Fourier Spectral Methods: second edition* (2000).

397 **Acknowledgements** The authors would like to thank Ze’ev Reches and two anonymous reviewers for their
398 constructive and fruitful comments that help the manuscript improve significantly. This work was supported
399 by the Southern California Earthquake Center (SCEC), award number 118062196. SCEC is funded by NSF
400 Cooperative Agreement EAR-1033462 and USGS Cooperative Agreement G12AC20038.

401 **Author contributions** MV and HR contributed to the development of the model. HR contributed to the
402 numerical implementation of the model and the comparison with experimental data. HR and MV contributed
403 to the writing of the paper.

404 **Competing Interests** The authors declare that they have no competing financial interests.

405 **Correspondence** Correspondence and requests for materials should be addressed to Hadrien Rattiez. (email:
406 hadrien.rattiez@duke.edu).

407 **Data availability** The experimental data used in Figure 3 are available in the supplementary information.

408 **Code availability** The numerical code used to simulate the results of the model is available from the

409 corresponding author upon request.